

NUMERICAL SIMULATIONS OF ASTROPHYSICAL JETS FROM KEPLERIAN DISKS. II. EPISODIC OUTFLOWS

RACHID OUYED¹ AND RALPH E. PUDRITZ²

Department of Physics and Astronomy, McMaster University, Hamilton, Ontario L8S 4M1, Canada

Received 1996 August 8; accepted 1997 February 27

ABSTRACT

We present 2.5-dimensional time-dependent simulations of the nonlinear evolution of nonrelativistic outflows from Keplerian accretion disks orbiting low-mass protostars or black holes accreting at sub-Eddington rates. The gas is ejected from the surface of the disk (which is a fixed platform in these simulations) into a cold corona in stable equilibrium. The initial magnetic field lines are taken to be uniform and parallel to the disk axis (z -axis). Because of the gradient force in the nonlinear torsional Alfvén waves generated by the rotor at the footpoints of the field lines, the initial magnetic configuration opens up in a narrow region on the disk's surface located at $r_i < r < 2r_i$ with r_i being the innermost radius of the disk. Within this narrow region, a wind is ejected from the field lines that have opened to less than the critical angle ($\simeq 60^\circ$), as expected from the centrifugally driven wind theory. Our simulations show that the strong toroidal magnetic field generated recollimates the flow toward the disk's axis and, through magnetohydrodynamic (MHD) shocks, produces knots. The knot generation mechanism occurs at a distance of about $z \simeq 8r_i$ from the surface of the disk. Knots propagate down the length of the jet at speeds less than the diffuse component of the outflow. The knot generator is episodic and is inherent to the jet.

Subject headings: accretion, accretion disks — galaxies: jets — ISM: jets and outflows — MHD

1. INTRODUCTION

One of the most challenging aspects of theories and models of astrophysical jets is to provide a natural explanation for common features such as the episodic outbursts and the knots observed in astrophysical jets. Among the models so far proposed are the magnetohydrodynamic (MHD) winds from a Keplerian disk (Blandford & Payne 1982, hereafter BP82; Uchida & Shibata 1985; Camenzid 1987; Pudritz & Norman 1986; Lovelace, Wang, & Sulkanen 1987; Heyvaerts & Norman 1989; Pelletier & Pudritz 1992; Appl & Camenzid 1992; Königl & Ruden 1993; Sauty & Tsinganos 1994 to cite only few). However, while the existing stationary wind models help us understand the basic physics of such winds (acceleration and collimation), they are limited by their assumptions of self-similarity and stationarity. Such assumptions are made because of the complexity of MHD equations one needs to solve. Numerical simulations are therefore a complementary step and a necessary tool in the study of astrophysical jets (Shibata & Uchida 1986; Kössl, Müller, & Hillebrandt 1990; Stone & Norman 1994; Bell & Lucek 1995; Ustyugova et al. 1995, to cite only few). In the first paper in this series (Ouyed & Pudritz 1997a, hereafter OPI), we introduced the reader to the general setup and the initial conditions corresponding to a central object surrounded by a Keplerian disk and an overlying cold corona in stable equilibrium. We presented an extended version of ZEUS-2D designed to overcome the numerical difficulties related the realization of this initial setup, as well as results for a steady state simulation using a simple initial potential ($J = 0$) field configuration.

In this paper, we present a complete study of a uniform vertical configuration, where the magnetic field lines are parallel to the disk's axis. This magnetic configuration was

chosen because it is the simplest one to study and is not expected to produce an outflow in steady state theory.

As before, our disk is treated as a boundary condition at the base of the outflow. The disk is kept in Keplerian rotation throughout the simulation. Our results are remarkable in that outflow is both self-initiated by toroidal magnetic field pressure generated in the jet which opens up the field lines and episodic in that it generates a large number of knots that continue to be produced for many disk dynamical timescales and grid crossing times. The knots originate near the compact object with temporal frequencies that roughly match the observations. Here, we present a sample of simulations from a dozen that we carried out over the last year that show that whereas some of the predictions of steady state models are borne out (OPI), there exist magnetic configurations that produce episodic jets, as the observations demand (Ouyed, Pudritz, & Stone 1997).

The paper is organized as follows: in § 2, we briefly remind the reader of our initial setup, that is, the state of the corona and of the overlying Keplerian accretion disk. In § 3, the development of the outflow and its interaction with the surrounding corona is presented in detail. Section 4 deals with the details of the knot generator, while § 5 investigates the physics behind the ejection and the acceleration mechanism. The strength and the energetics of our outflow are presented in § 6. Finally, a summary of our results and a conclusion are given in § 7 with an emphasis on the importance of our work in the general scheme of outflows from young stellar objects (YSOs) and active galactic nuclei (AGNs).

2. DIMENSIONLESS VARIABLES AND INITIAL SETUP

We refer the reader to OPI for the discussion of the analytical equations describing the physics of the magnetized astrophysical flows and of accretion disks dealt with here. The model consists of a point mass representing a star or black hole; the *surface* of a surrounding accretion disk that

¹ ouyed@physics.mcmaster.ca.

² pudritz@physics.mcmaster.ca.

is taken to have an inner radius r_i (this can be either the surface of the star, the magnetopause radius of a star with the disk, or the last stable Kepler-like orbit around a black hole); an initial disk corona that is in hydrostatic equilibrium within the gravitational field of the central object as well as in pressure balance with the disk below; and an initial magnetic field that threads the disk and corona. The gas is taken to be a polytrope of index $\gamma = 5/3$. We adopt cylindrical coordinates (r, ϕ, z) with the origin at the central object and take the z -axis to be perpendicular to the disk, such that the surface of the disk lies in the $z = 0$ plane of our coordinate system. We chose a dimensionless form in which the quantities are given in units of their values at r_i . The footpoint of a given field line on the disk is denoted r_0 . In general then, we define our dimensionless variables as

$$r' = \frac{r}{r_i}, \quad z' = \frac{z}{r_i}, \quad v' = \frac{v}{v_{K,i}}, \quad \rho' = \frac{\rho}{\rho_i},$$

$$B' = \frac{B}{B_i}, \quad \Phi' = -\frac{1}{\sqrt{r'^2 + z'^2}}, \quad \nabla' = r_i \nabla, \quad (2.1)$$

where $v_{K,i} = (GM/r_i)^{1/2}$ is the Kepler speed at r_i and B_i is the poloidal field at r_i . Time is given in units of $t_i = r_i/v_{K,i}$, so that the dimensionless time is

$$\tau = \frac{t}{t_i}. \quad (2.2)$$

The results can therefore be scaled to a central object of any desired mass (refer to Tables 1 and 2 in OPI).

From now on, and for simplicity, we drop the primes keeping in mind that our quantities henceforth represent dimensionless variables.

2.1. Cold Corona

We set the initial toroidal field component B_ϕ and gas velocity everywhere in the corona equal to zero, with the additional constraint that the corona is initially current free, i.e., $\mathbf{J} = \nabla \times \mathbf{B} = 0$. We avoid the use of a softening parameter for the (Newtonian) potential. We then find that unless one carefully establishes a disk corona that is in numerical hydrostatic equilibrium, the resulting gas motions (such as collapse of the corona) interact strongly with the launch of the outflow resulting in spurious transients that strongly affect the subsequent evolution.

Cold coronae can be supported by turbulent pressure (possibly originating from the Balbus-Hawley instability [Balbus & Hawley 1991, hereafter BH] in the underlying disk). We incorporated this into our calculations and assumed that the effective turbulent pressure scales in proportion to the thermal pressure (OPI). The equilibrium condition for such “cold” coronae is then $h_{\text{eff}} + \phi = \text{const}$ (where h_{eff} is the effective enthalpy of the gas). This determines the initial gas density at every point as

$$\rho = \left(\frac{1}{\sqrt{r^2 + z^2}} \right)^{2/3} \quad (2.3)$$

with

$$\rho_i = \frac{\beta_i \delta_i}{2} \frac{B_i^2 / 4\pi}{v_{K,i}^2}. \quad (2.4)$$

The corona is defined by the following parameters:

$$\delta_i = \gamma \frac{v_{K,i}^2}{c_{s,i}^2}, \quad (2.5)$$

which is the ratio of Kepler to thermal energy density, and

$$\beta_i = \frac{8\pi p_i}{B_i^2}, \quad (2.6)$$

which is the ratio of the gas to the magnetic pressure at the innermost radius of the disk.

2.2. Initial Magnetic Configuration

In this paper, a vertical configuration is used with the initial surfaces of constant magnetic flux prescribed by the level surfaces of a scalar function (given in units of $r_i B_i$)

$$A_\phi = r. \quad (2.7)$$

That is,

$$B_z = 2.0 \quad \text{and} \quad B_r = 0.0. \quad (2.8)$$

While our vertical magnetic configuration was chosen to overcome some mathematical difficulties, we feel that it is still a good starting model for the kind of problems we are investigating in this paper. Indeed, it is possible for such a configuration to be created in a situation in which accretion flow into a turbulent disk (of high magnetic Prandtl number) drags an external magnetic field into the central object from the surrounding medium (Lubow, Papaloizou, & Pringle 1994; Reys-Ruis & Stepinski 1996).

The initial radial and vertical magnetic field components in the disk are continuous with the field in the corona (see OPI for more details). That is, the magnetic structure penetrates the disk (described below) and the overlying corona without any kink in the initial magnetic configurations that might introduce some undesired spurious effects (due to current sheets).

2.3. Disk Surface

The Keplerian accretion disk surface (the base of the corona) provides fixed boundary conditions for the velocity at every disk radius; the rotational speed is Keplerian v_K . Note that a subscript “ d ” stands for disk and “0” for coronal quantities at $z = 0$. The disk is defined by the last two free parameters in our model, namely,

$$\eta_i = \frac{\rho_{d,i}}{\rho_{c,i}}, \quad (2.9)$$

which is the disk-to-corona density ratio and

$$\mu_i = \frac{B_{\phi,i}}{B_{z,i}} \Big|_{z=0}, \quad (2.10)$$

which measures the toroidal-to-poloidal field ratio at the disk surface. The toroidal field in the disk is always taken to scale with disk radius as

$$B_\phi = \frac{\mu_i}{r}, \quad (2.11)$$

while the poloidal field is given by equation (2.8) for $z < 0$. The disk’s density is given as

$$\rho_d = \eta_i \rho_0 = \eta_i r^{-3/2}, \quad (2.12)$$

while

$$\beta_d = \frac{(\gamma - 1)}{\gamma} \delta_i \beta_0 \quad (2.13)$$

with

$$\beta_0 = \beta_i r_0^{-5/2}. \quad (2.14)$$

Note that equation (2.13) implies that β_d falls from the innermost value of $(\gamma - 1)/\gamma \delta_i \beta_i$ to an outermost value of $[(\gamma - 1)/\gamma] \delta_i \beta_i r_e^{-5/2}$. The disk radius at which β_d is unity is simply given as

$$1 = \frac{(\gamma - 1)}{\gamma} \delta_i \beta_i r_1^{-5/2} \quad (2.15)$$

or

$$r_1 = (\frac{2}{5} \delta_i \beta_i)^{2/5}. \quad (2.16)$$

Interior to r_1 , we expect both global and local modes of the BH instability to be present, while the linear stage of this instability will dominate in the regions interior to r_1 . But, again, because we treat the disk simply as a boundary condition at the base of the corona, we cannot study how the instability will affect the acceleration of the outflow (see OPI).

2.4. Timescales

We showed that there are three important timescales defined at the disk's surface, $t_x = r/v_x$, where v_x is the velocity of the wave considered. These are the Kepler time τ_K , the Alfvén time τ_A , and the magnetic braking time τ_B , which is the time it would take a torsional wave propagating onto the external medium to traverse an amount of material whose moment of inertia is the same as the moment of inertia of the disk. We showed that

$$(\tau_K, \tau_A, \tau_B) = (1, \sqrt{\delta_i \beta_i / 2}, \eta_i \sqrt{\delta_i \beta_i / 2}). \quad (2.17)$$

2.5. Parameters and Boundary Conditions

The set of five free parameters in our model consists of $(\delta_i, \beta_i, \eta_i, \mu_i, v_{inj})$, where $v_{inj} = v_p/v_K$ is the dimensionless injection velocity and v_p is the poloidal velocity at the disk's surface. We use open boundaries to avoid any artificial colimation due to reflective boundaries. We use inflow boundary conditions at the disk surface (except for the magnetic field for which we use open boundaries, so that it evolves through the $\nabla \cdot \mathbf{B} = 0$ constraint) and open outflow conditions (i.e., *zero normal gradient*) on the remaining boundaries (except along the axis of symmetry, coinciding with the disk axis, taken to be reflecting; i.e., *the normal components of velocity and magnetic field are reflected, while the tangential components are continuous*). Because of the axisymmetry, we compute in only one quadrant. Figure 2 in OPI illustrates the initial setup and the open boundary mesh.

The conditions describing the central object and the accretion disk surface are set in the so-called ghost zones and are fixed once and for all. In all our simulations, the gas is injected from the ghost zones into the active zones (the corona) at a velocity³ $v_p = 10^{-3} v_K$ with $v_p \parallel \mathbf{B}_p$. Introducing the launching angle $\theta_0 = \tan(B_r/B_z)$, the velocity field in the

ghost zone is

$$\mathbf{v} = (v_r, v_\phi, v_z) = [v_p \sin(\theta_0), v_K, v_p \cos(\theta_0)] \quad \text{if } r \geq 1 \quad (2.18)$$

$$= (0, 0, 0) \quad \text{if } r < 1. \quad (2.19)$$

The second constraint incorporates a region interior to r_i (which might be an empty magnetosphere or simply a slowly rotating object) in which the disk is absent. The rest of the parameters are set through equations (2.9), and (2.10).

3. EVOLUTION OF THE OUTFLOW

Our first simulation (simulation A) was run in the domain $(z, r) = (80, 20)$ with a resolution of (500, 200) cells, for up to 500 time units ($< \tau_B$). This allows us to have a more global look at the jet and its interaction with the corona, reasonably far from the central object. The set of parameters is

$$(\delta_i, \beta_i, \eta_i, \mu_i, v_{inj}) = (100.0, 1.0, 100.0, 1.0, 0.001) \\ \Rightarrow (\tau_K, \tau_A, \tau_B) = (1.0, 7.07, 707.1). \quad (3.20)$$

3.1. Magnetic Torque and the Generation of Torsional Alfvén Waves

Here, we briefly review the notion of torsional Alfvén waves as they first appear in our simulation (Fig. 1). Below, we describe the two distinct regions that separate the linear regime from the nonlinear one. The latter one occurs in the innermost parts of the disk where $(B_\phi/B_p)_i = 1$ to start with and where the winding of the field line (through v_ϕ) is also the strongest. As one goes radially outward, B_ϕ decreases sharply with radius ($B_\phi \propto r^{-1}$) and so is $v_\phi \propto r^{-1/2}$ making $B_\phi/B_p < 1$.

3.1.1. Linear Regime ($\delta\rho = 0$ with $B_\phi/B_p \ll 1$)

The linear regime of propagation of torsional waves is presented in Mouschovias & Paleologou (1980). Such a regime is seen in the early times ($\tau \leq 50$)⁴ of the simulation, far from the source where gravity can be neglected.

To illustrate that, let us start with the flux-freezing equation. Since we initially have $\mathbf{B}_p = (0, 0, B_z)$, then

$$\frac{\partial \mathbf{B}_\phi}{\partial \tau} = r(\mathbf{B}_p \cdot \nabla) \Omega = r B_z \frac{\partial \Omega}{\partial z}. \quad (3.21)$$

The ϕ component of the magnetohydrodynamic force equation is

$$\frac{\partial \Omega}{\partial \tau} = \frac{2}{\beta_i \delta_i} \frac{B_z}{4\pi r \rho_{\text{ext}}} \frac{\partial B_\phi}{\partial z}. \quad (3.22)$$

Combined with the equation above, we obtain

$$\frac{\partial^2 \Omega}{\partial \tau^2} = \frac{2}{\beta_i \delta_i} v_{A, \text{ext}}^2 \frac{\partial^2 \Omega}{\partial z^2}. \quad (3.23)$$

Similarly one can show that

$$\frac{\partial^2 B_\phi}{\partial \tau^2} = \frac{2}{\beta_i \delta_i} v_{A, \text{ext}}^2 \frac{\partial^2 B_\phi}{\partial z^2}, \quad (3.24)$$

which is the equation for propagation of linear torsional waves in the external medium. Notice that such a situation occurs because of the existence of the gradient of Ω along

³ The injection velocity is taken to be the hundredth of the disk's sound speed (OPI).

⁴ This is the time during which v_z is negligibly small (compared with the Alfvén velocity). One can show that velocities in the radial direction also vanish, as found in the outermost regions of the disk. It then follows from flux freezing that B_r and B_z are constants of the motion [$B_r(\tau) = 0$ and $B_z(\tau) = \text{const}$].

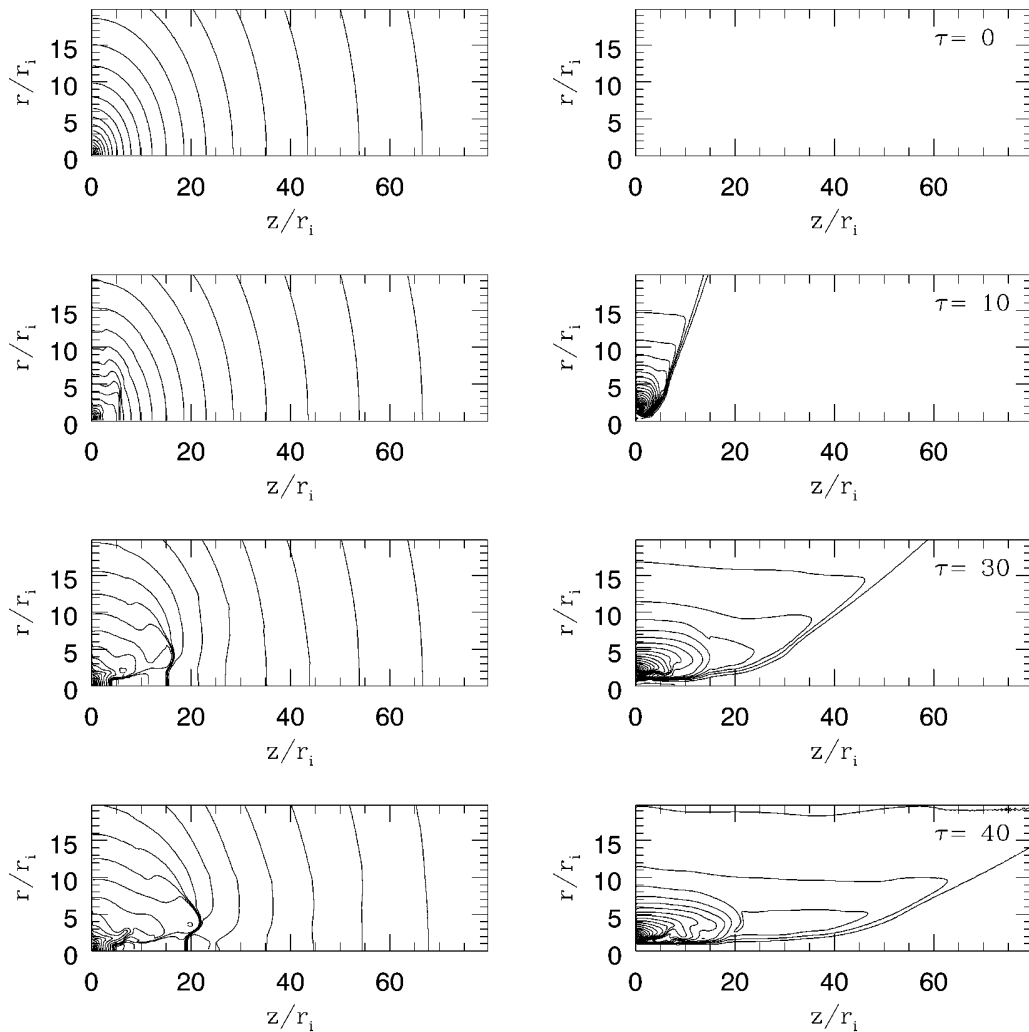


FIG. 1.—Evolution of the density (isocontours shown in the left-hand panels) and the toroidal magnetic field (isocontours shown in the right-hand panels) showing the propagation of the initial torsional Alfvén waves. The initial density distribution, as given by eq. (2.3), is shown in the upper left-hand panel. Initially, $B_\phi = 0.0$ in the corona (upper right-hand panel). The mesh is $(z \times r) = (80 \times 20)r_i$ with a resolution of (500×200) zones. The evolution is shown at four different times: $\tau = 0$, $\tau = 10$, $\tau = 20$, and $\tau = 40$ from top to bottom. Twenty logarithmically spaced contour lines are shown for the density, and 20 linearly spaced contours for B_ϕ . In this figure (and in all the figures), the axis of symmetry is plotted horizontally and the equatorial plane vertically. Note because of axisymmetry we only compute in one quadrant.

the flow axis (z) that corresponds to our initial equilibrium. Here, because $v_{A, \text{ext}} \propto (r^2 + z^2)^{3/8}$, torsional waves starting at different footpoints will travel into the external medium at different velocities. This gives rise to the conical shape of the Alfvén front, as is clearly seen in Figure 1 (the fastest wave starts from the outermost radius of the disk). A direct application of equation (3.24) implies that

$$\tau \simeq \sqrt{\frac{\pi}{2}} \beta_i \delta_i \frac{z}{(r^2 + z^2)^{3/8}}. \quad (3.25)$$

That is, a wave leaving the disk surface at $r_0 = 20r_i$ should leave the mesh ($z_e = 80r_i$) at about $\tau \simeq 35.0$. This is in good agreement with our solution (Fig. 1).

3.1.2. Nonlinear Regime ($\delta\rho \neq 0$ with $B_\phi/B_p \geq 1$)

Very close to the central object, nonlinear torsional Alfvén waves (see § 5 and related figures for details) generate a strong gradient of magnetic pressure $\nabla(B_\phi^2)$. In fact, the boundary between the linear and the nonlinear region ($B_\phi/B_p \simeq 1$) can be followed as the flow evolves in time. In general, in the region of the corona, where only linear waves

are launched, the density remains undisturbed and conserves its initial distribution. In the region where nonlinear torsional Alfvén waves are generated, the density is somewhat affected by the toroidal field. Later in the evolution of the outflow, a jetlike outflow is produced that eventually catches up with the Alfvén front.

3.2. Onset and Evolution of the Outflow

Figure 2 shows the evolution of the flow at $\tau = 100$, $\tau = 200$, $\tau = 300$, and $\tau = 400$. According to steady state models (BP82; Königl 1989; Ferreira & Pelletier 1995; Wardle & Königl 1993; Li 1995), our initial magnetic configuration is unfavorable for launching an outflow. The flow is nonetheless launched from the accretion disk (see § 5). In this figure, the density is shown in the left-hand panels, while the toroidal magnetic field is in the right-hand panels.

The jetlike flow has a density structure that is dominated by discrete knots that are part of a highly collimated flow. At times 100 and 200, the head of the outflow is clearly seen. It advances into the flow with a swept-back material shock emanating from its flanks. This surface leaves our grid long before 400 time units.

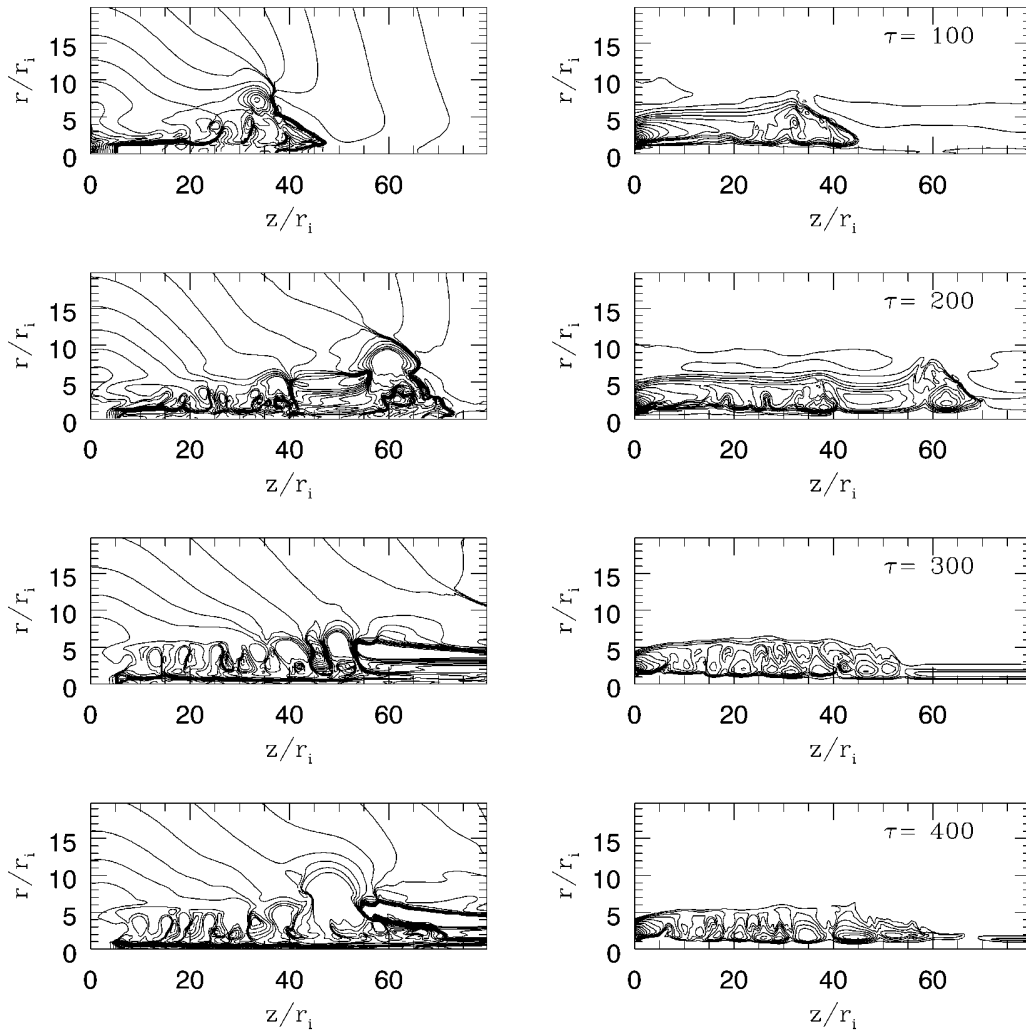


FIG. 2.—Evolution of the density (isocontours shown in the left-hand panels) and the toroidal magnetic field (isocontours shown in the right-hand panels) showing the evolution of the episodic outflow. The mesh is $(z \times r) = (80 \times 20)r_i$ with a resolution of (500×200) zones. The evolution is shown at four different times: $\tau = 100$, $\tau = 200$, $\tau = 300$, and $\tau = 400$ from top to bottom. Twenty logarithmically spaced contour lines are shown for the density, and 20 linearly spaced contours for B_ϕ .

The density structure *never* achieves steady state. We have run simulations for up to 1000 time units and find that the episodic nature of the flow persists unabated. The density contours show that our jet is more highly collimated and narrow. This again shows that the outflow region is strongly confined near the axis (but off the axis since our jet is a hollow one)⁵ but that there is a larger, lower density region surrounding the jet on larger radial scales. The map of the associated toroidal field in the flow reveals that the toroidal field is strongly *anticorrelated* with the knots. Generally speaking, high-density knots are associated with regions of low toroidal field strength. Such structures have been seen in pure MHD jet simulations (Clarke, Norman, & Burns 1986; Lind et al. 1989) where magnetized jets are launched into a uniform medium through a narrow orifice.

In Figure 3, we show the evolution of the poloidal magnetic field (*left-hand panels*) and of the launching angle θ_0 (*right-hand panels*). The initially vertical configuration opens up very close to the central object, which allows for a gas to be ejected into the corona above. A closer look deep

into the central gravitational well (see § 4) reveals that only a tiny fraction of the field lines get opened up and participates in the outflow. As the small knots move away from the disk surface, they interact with bigger knots formed further down the stream. Numerical reconnections (refer to Fig. 3) occur within the large knots (at $z \simeq 60\text{--}70r_i$, we see reconnections occurring), but they quickly dissipate as they leave the mesh allowing a smoother magnetic configuration. Note, however, that the field lines are well behaved away from the complex and complicated large knots.

Figure 4 shows the complexity of the vector velocity around the knots. In particular, there is evidence for gas backflowing along the flank of the working surface. The high-velocity feature seen in the center or the large knots are probably produced by the numerical reconnections that disappear later in the evolution of the jet. Around the small knots, there is a clear evidence of collimation and decollimation of the jet due to the confining effects of the toroidal magnetic field.

3.2.1. Knots

Recent observational studies of knots in a few jets were carried using narrow-band CCD imaging (Eislöffel &

⁵ The narrow region is only $1r_i$ in radius (0.04 AU for our fiducial $0.5 M_\odot$ YSO). Such a narrow region would be difficult to resolve, however.

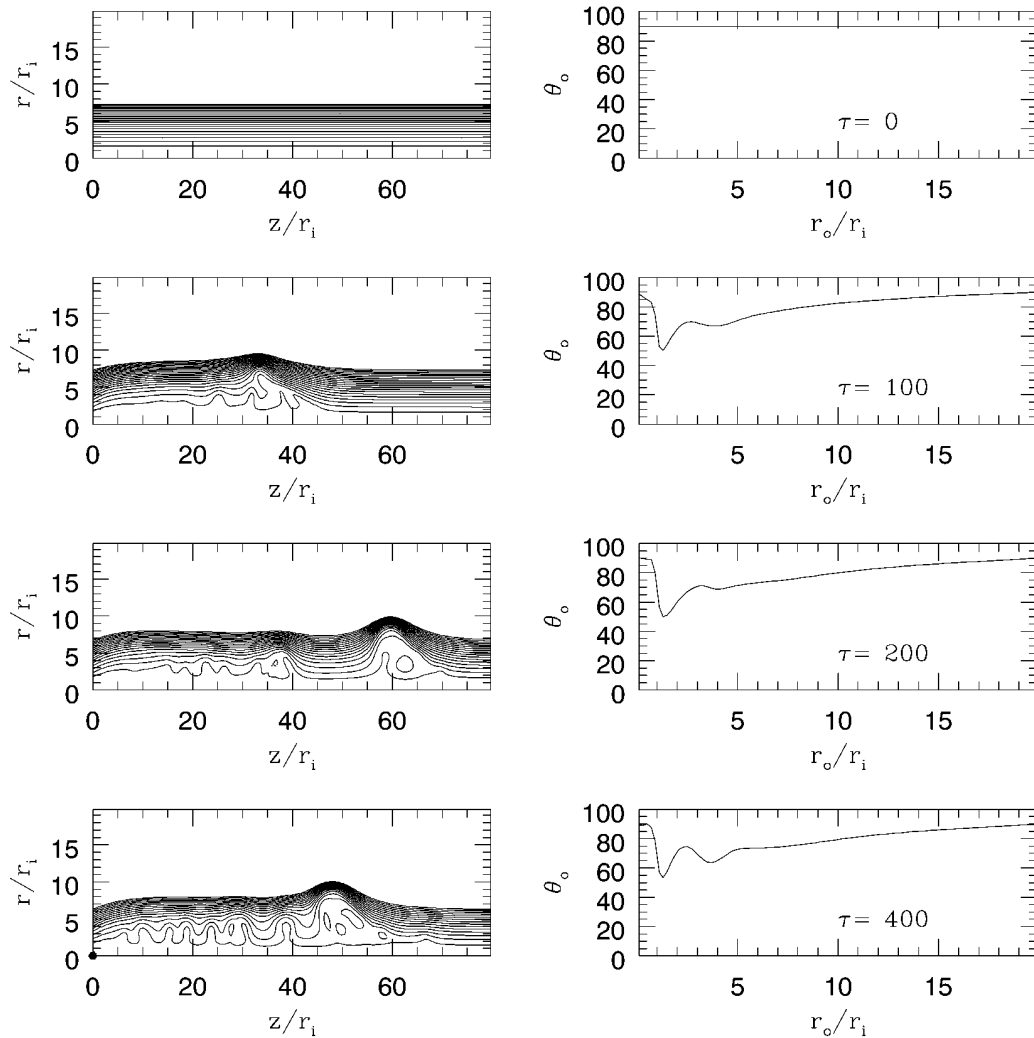


FIG. 3.—Evolution of the poloidal magnetic field (*left-hand panels*) and the launching angle at the disk's surface (*right-hand panels*). The initial magnetic potential configuration, as given by eq. (2.7), is shown in the upper left-hand panel. The mesh is $(z \times r) = (80 \times 20)r_i$ with a resolution of (500×200) zones. The evolution is shown at four different times: $\tau = 0$, $\tau = 100$, $\tau = 200$, and $\tau = 400$ from top to bottom.

Mundt 1994). These studies showed that practically all knots in jets move with tangential velocities comparable to measured radial velocities, and therefore any models explaining the knots by stationary shocks can be excluded. Furthermore, the ratio of the knot pattern speed relative to the fluid speed was measured to be between 0.2 and 1, with tangential velocities of the knots between 100 km s^{-1} to more than 300 km s^{-1} .

From our simulation, the velocity of the knots is lower than that of the diffuse material between the knots, a property that corresponds well with the above observations. The typical ratio of the velocity in the knots to that of the diffuse jet material is 0.3–0.5, with the highest outflow velocities about equal to $v_{K,i}$. Although this velocity is not as large as is sometimes observed in real outflows such as that in HH30 (Reipurth 1989), our simulations explore only a limited region of parameter space. Movies of this simulation show that the knot generator stays fixed in space and that the knots, once formed, persist as coherent structures that propagate down the length of the jet.

Figure 5 is a density cut, taken at $r_o = 3r_i$, along the body of the knots. At $\tau = 100$, we clearly discern the bow shock. The typical density jumps in the knots are ≤ 4 . Some of the

small knots continue to evolve as a shock discontinuity, while others combine to form larger knots at $z \simeq 60r_i$ above the disk's surface; we estimate that the knot is $\simeq 10r_i$ in radius. The first large knot forms at $\tau = 200$ and then propagates down the length of the jet as a separate entity. At $\tau = 400$, another large knot is formed at the same location as the previous one and evolves in a similar way. It is interesting to note that the region between the two large knots becomes very sparse in gas and is characterized by a smooth monotonically increasing velocity profile (a consequence of mass conservation). This region is clearly seen at $\tau = 300$ at $40r_i < z < 80r_i$ (refer to Figs. 2, 3, and 4).

In general, then, we find two types of knots that can be summarized as follow:

1. *Small knots.*—The smaller knots are typically *separated* by a distance of $\simeq 5r_i$, and their size is of the order of $\simeq 5r_i$ in radius. These knots are produced every $11t_i$. These knots start as shocks, and some of them evolve as shocks until they dissipate when they encounter the larger knots described below.

2. *Large knots.*—The larger knots appear to be more slowly moving structures that build up by absorbing some

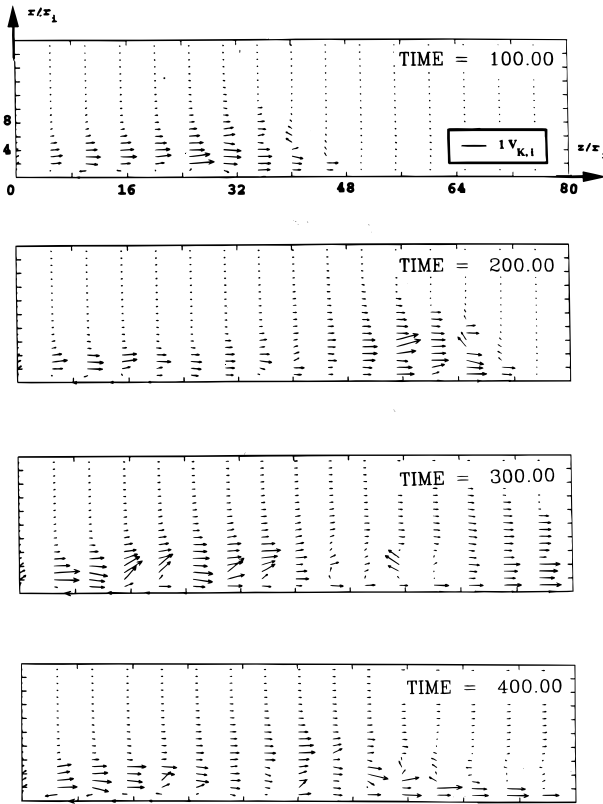


FIG. 4.—Poloidal vector velocity v_p at $\tau = 100$, $\tau = 200$, $\tau = 300$, and $\tau = 400$, respectively, from top to bottom.

TABLE 1
KNOT FEATURES

Parameter	Small Knots	Large Knots
$z_{\text{Generator}}$	$\simeq 8r_i$	$\simeq 60r_i$
Size (radius).....	$\simeq 5r_i$	$\simeq 10r_i$
Δz_{knot}	$5r_i$	$15r_i$
$v_{\text{knot}}/v_{\text{jet}}$	0.3–0.5	0.1–0.3
Δt_{knot}	11–13 t_i	150–200 t_i

TABLE 2
KNOT FEATURES: APPLICATION TO YOUNG STELLAR
OBJECTS (PROTOSTAR [$0.5 M_\odot$])

Parameter	Small Knots	Large Knots
$z_{\text{Generator}}$ (AU)	0.3	2.4
Size (radius, AU).....	0.2	0.4
Δz_{knot} (AU)	0.2	0.6
v_{knot} (km s $^{-1}$).....	60.0	40.0
Δt_{knot} (days)	7.2	105.0

TABLE 3
KNOT FEATURES: APPLICATION TO ACTIVE GALACTIC
NUCLEI (BLACK HOLE [$10^8 M_\odot$])

Parameter	Small Knots	Large Knots
$z_{\text{Generator}}$ (AU)	164.8	1237.0
Size (radius, AU).....	103.1	206.2
Δz_{knot} (AU)	103.1	309.0
v_{knot} (km s $^{-1}$).....	3.0×10^4	2.0×10^4
Δt_{knot} (days)	6.4	92.7

of the more quickly moving knots produced at the generator. Some of the small knots go through the first large knot and form another larger knot farther down the flow. These larger knots are typically *separated* by a distance of $\simeq 15r_i$, and their size is of the order of $\simeq 10r_i$ in radius. They are generated at $z \simeq 60r_i$ above the disk's surface and are produced every $200t_i$.

We summarize in Table 1 the general results cited above. Tables 2 and 3 give the numbers for our fiducial parameters as applied to a typical $0.5 M_\odot$ YSO and a typical $10^8 M_\odot$ AGN, respectively.

4. THE KNOT GENERATOR

For the same set of parameters as in simulation A, we performed a second simulation (simulation B). It was run, in the domain $(z, r) = (20, 10)$ with a resolution of (500, 200) cells, for up to 50 time units ($< \tau_B$). The purpose of simulation B is to give a close-up view of the physics of flow acceleration and knot generation.

In Figure 6, we show the magnetic field configuration of the outflow at times 37.2, 40.8, 44.4, and 48.0 during which a knot (B) is formed (knot A moves away from the generating region as knot B is formed). This whole process takes a time $\tau_{\text{knot}} \simeq 11$ time units. The knots are *spatially* separated by a distance of $z \simeq 5r_i$ (confirming the results found in the large-scale simulation) and move at a speed of $\simeq 0.5v_{k,i}$ out of this generating region. This figure is complementary to Figure 5 in Ouyed et al. (1997, to which we refer the reader), where it is clearly seen that both knots are produced at a distance of

$$6r_i \leq z_{\text{Generator}} \leq 8r_i \quad (4.26)$$

from the central object. Once formed, the shocked gas (see below) comprising knot A appears to detach from the inner velocity stream (see the lower panels in Fig. 5 of Ouyed et al. 1997) and moves down the jet. *The high toroidal magnetic field strength between the knots provides the confining pressure that allows the knots to remain as distinct entities* (as seen in Fig. 7c).

4.1. How Are the Knots Generated?

There are various attempts in the theory literature to identify the knot spacings with the resonant wavelength pinch mode. While some of the conditions in our knot generating region seem to point toward such a scenario (in particular the high B_ϕ/B_z ratio), we are nonetheless able to rule it out by comparing simulations at different β (Ouyed & Pudritz 1997b). Indeed, we found that simulations with even lower value of β_i do not produce knots, which is not what one would expect if they were pinch mode instabilities (in fact, we find that only when β_i is around unity are knots produced). We have not encountered any of the pinching instabilities for our choice of parameters, which confirms several results in the literature. For example, we confirm the result of Appl & Camenzid (1992) that the axisymmetric ($m = 0$) mode is entirely stabilized for low- β , current-carrying, cylindrical jets (our case). Kelvin-Helmholtz instabilities are also ruled out as an explanation for knot generation for two reasons. First, the flow is super-Alfvénic, a regime that should be quite stable (Birkinshaw 1990), and second, as already mentioned above, simulations we performed at even higher values of β do not produce knots.

We find that the knots are initially produced in shocks in a region of the flow beyond the Alfvén surface (marked on

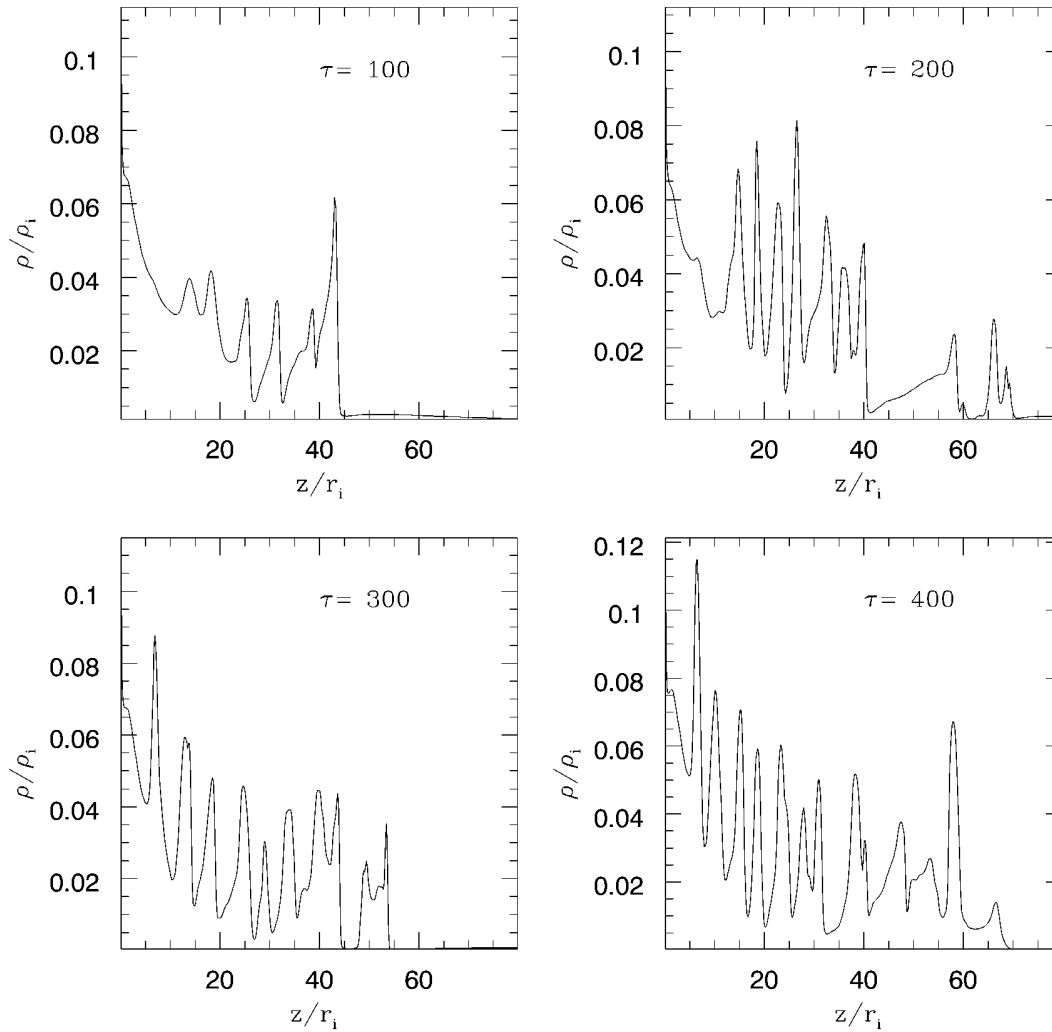


FIG. 5.—Density (ρ) cut parallel to the z -axis. The cut is taken directly in Fig. 1, at $r_0 = 3r_i$. This figure illustrates the values of the contour levels as well as the jet to the ambient density ratio during the evolution of the outflow. The evolution of the knots can be seen with some of the small knots turning into shocks further down the jet. The complex structure of the large knots, located at $\approx 60r_i$, is also seen. The size of a typical large knot is $\approx 10r_i$ in radius.

the field lines in Fig. 6) in the outflow, around $z_{\text{Generator}} \approx 6-8r_i$. Cuts of density (Fig. 7a), v_z (Fig. 7b), and $|B_\phi|$ (Fig. 7c), taken parallel to the z -axis at $r_0 = 3r_i$ (along the body of the jet), reveal more information on the physics of the knots. These figures clearly show the location of the knot generator at about $z \approx 8r_i$. The density jump associated with a decrease in velocity and an increase in the poloidal magnetic field (see the corresponding number in Table 4) is a strong indication of fast MHD shocks (Oued & Pudritz 1994; hereafter OP94). In such shocks, the kinetic energy of the flow is converted into both magnetic energy (amplifying the field) and thermal energy. When superimposed, Figures 7a and 7c confirm the anticorrelation between the density and the toroidal magnetic field and the fact that the knots are confined between regions of strong B_ϕ .

TABLE 4

KNOT FEATURES: JUMP IN PHYSICAL QUANTITIES

Knot	$V_{p,2}/V_{p,1}$	$V_{\phi,2}/V_{\phi,1}$	$B_{p,2}/B_{p,1}$	$B_{\phi,2}/B_{\phi,1}$	ρ_2/ρ_1
A.....	0.78	1.22	5.0	0.6	2.2
B.....	0.55	1.37	5.0	0.7	2.0

One important property we found is the spin-up of the jet material crossing the shocks (Table 4). This is simply due to the conservation of angular momentum

$$l = rv_\phi + \frac{r|B_\phi|}{k}, \quad (4.27)$$

with $k = \rho v_z/B_z$. Thus, any decrease in B_ϕ (as it happens across the shock)⁶ must be followed by an increase in v_ϕ . This result is similar to what was found by Kössl et al. (1990),⁷ but there is an important difference; the absolute value of v_ϕ they obtain is much smaller than the sonic velocity throughout their simulation. Therefore, the influence of the rotation on the propagation of the jet is almost negligible. In our case, the outflow is mainly in rotation to start with. The shock spins it up by no more than a factor of 1.4 in the strongest jumps.

⁶ It is straightforward to show that k is a constant across the shock (eqs. [3.21] and [3.22] in Oued & Pudritz 1993).

⁷ These authors studied the evolution of jets in helical magnetic field configurations and found that the maximum values of the toroidal velocity can be observed downstream the terminal Mach disk (see their Figs. 17–19). The acceleration of the jet material in ϕ direction is due to the angular momentum generated by a gradient in $B_p B_\phi$.

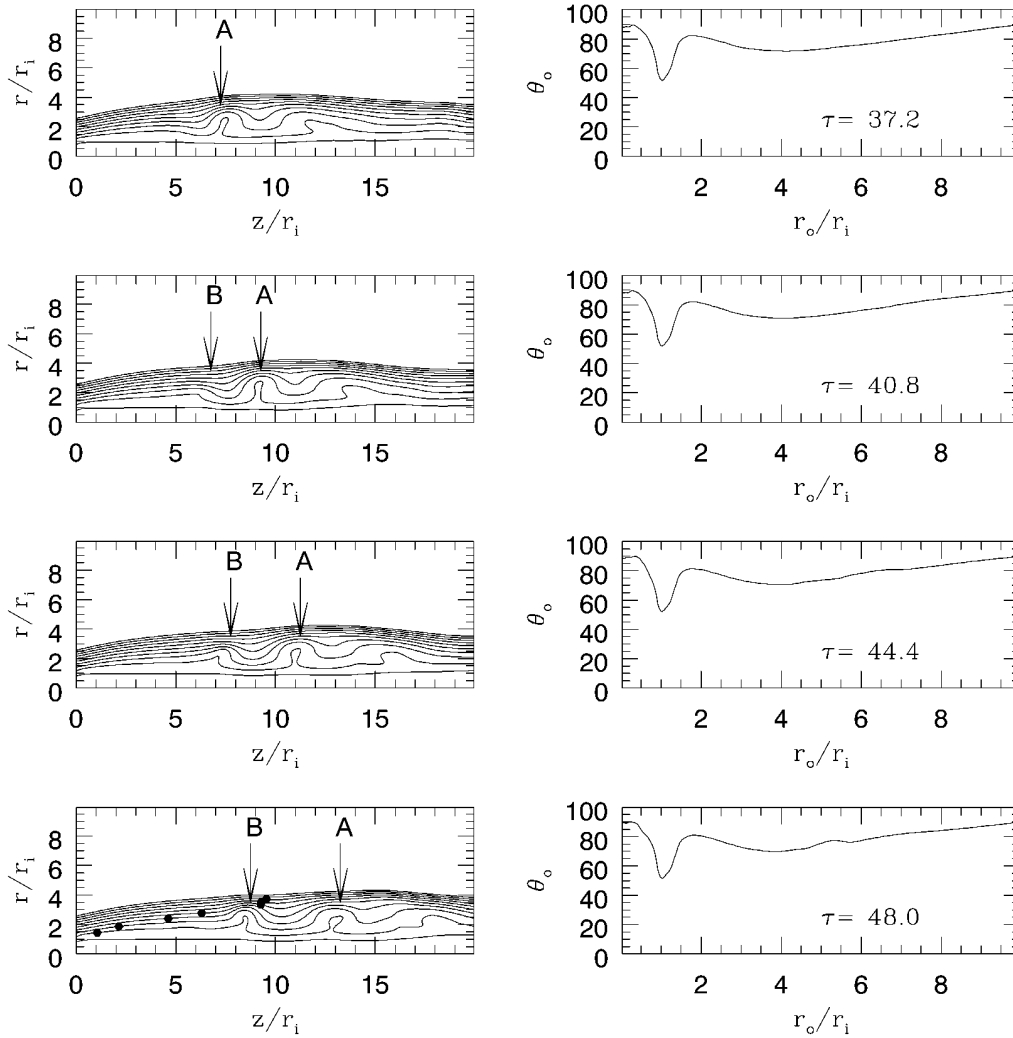


FIG. 6.—Simulation B. The left-hand panels show the magnetic field structure of the knot generating region, at the four times 37.2, 42.6, 44.0, and 48.0 inner time units. The right-hand panels show the angle θ_0 of field lines at the disk surface, at these times. Note the narrow band of field lines that is sufficiently opened ($\theta_0 \leq 60^\circ$) so as to drive the outflow. Only field lines involved in the knot generation process are shown; field lines at larger disk radius stay reasonably vertical as seen in the right-hand panels.

Our result is interesting in view of recent investigations of line profiles emerging from the vicinity ($3r_i < r < 12r_i$) of YSOs. In the case of FU Orionis, Calvet et al. (1993) showed that absorption features of observed lines are likely to form in a differentially expanding wind which is rapidly rotating. Rotational velocities of about $60\text{--}70 \text{ km s}^{-1}$ are needed in their models to fit the observed profiles. Here, we found the highest rotational velocity no more than $0.8 v_{K,i}$ (76 km s^{-1} for a $0.5 M_\odot$ protostar, like FU Orionis).

The question one can ask now is: why and how does the first shock come about? By looking at the distribution of the magnetic pressure associated with the self-generated toroidal field in the narrow band of outflowing, we see that the pressure force (∇B_ϕ) acts both radially outward and inward toward the axis. Hence, the accelerating outflow, on encountering the inwardly directed pressure gradient, is reflected back toward the axis. Now, because the outflow is rotating, the gas spins up as it moves inward and reflects off an inner “centrifugal barrier” when it reaches a radius comparable to its footpoint radius, as Figure 8 clearly shows (the poloidal vector velocity in Fig. 8 shows that the flow recollimates toward the axis and then reflects back into the

slower moving body of the jet). The resulting nearly harmonic oscillation has been predicted by Sauty & Tsinganos (1994). In our case, however, the corresponding variations in flow speed rapidly steepen into fast MHD shocks. Estimating that the toroidal Alfvén speed in our simulation is

$$v_{A,\phi} \simeq 0.5 - 0.6 v_{K,i}, \quad (4.28)$$

and the width of the jet to be

$$\delta r_j \simeq 3 - 4 r_i, \quad (4.29)$$

the oscillation period of the jet is

$$t_{\text{osc}} = 2\delta r_j / v_{A,\phi} \simeq 11 - 13 t_i, \quad (4.30)$$

which is indeed the knot measured production time scale in our simulation. By contrast, the initial magnetic pressure in the steady flow case (see OPI) drops significantly as one moves outward from the axis. Thus, the accelerating outflow does not encounter a strongly magnetically overpressured outer barrier and continues to expand radially, finally achieving a quiet, cylindrically collimated state.

To summarize this section, we found that knots are produced very close to the source, at a distance from the central

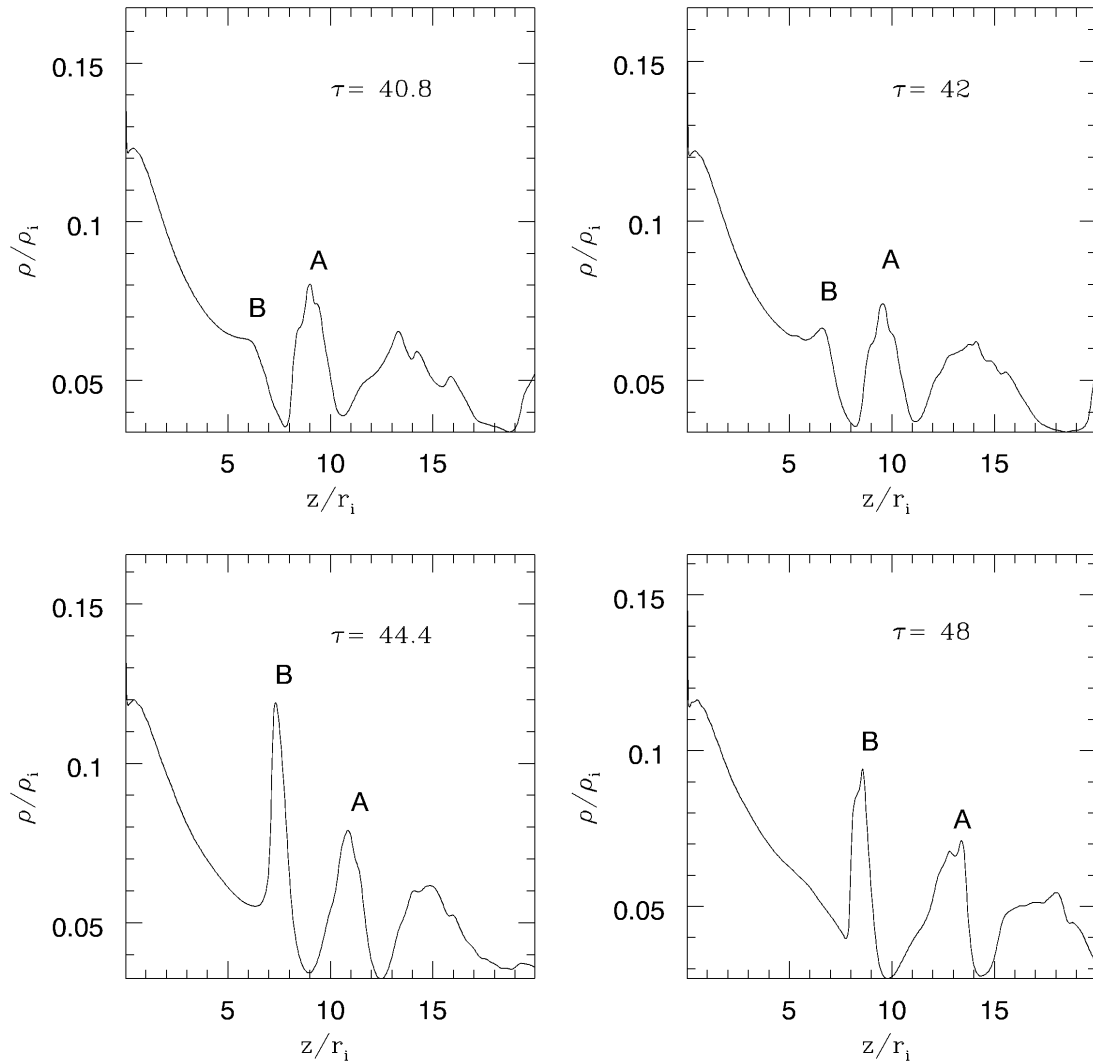


FIG. 7a

FIG. 7.—(a) Density (ρ) cut parallel to the disk's axis. The cut is taken directly in Fig. 6, at $r_0 = 3r_i$. This figure illustrates the values of the contour levels as well as the jet to the ambient density ratio during the evolution of the outflow. The production/evolution of knot A and knot B are also shown. (b) v_z cut parallel to the disk's axis. The cut is taken directly in Fig. 6, at $r_0 = 3r_i$. The production/evolution of knot A and knot B are also shown. (c) $|B_\phi|$ cut parallel to the disk's axis. The cut is taken directly in Fig. 6, at $r_0 = 3r_i$. The production/evolution of knot A and knot B are also shown.

source of about $7r_i$. Simulation B shows that the knot generation is inherent to the dynamics of the jet itself.⁸ It also shows that the knot generator stays fixed in space and that the knots, once initially formed as fast MHD shocks, persist as coherent structures that propagate down the length of the jet.

5. THE OUTFLOW AND ACCELERATION MECHANISM

We have shown in Figure 6 that a narrow region of field lines in the innermost parts of the disk is opened up, making an angle of 50° – 60° with respect to the disk surface. This narrow region, located at $r_i < r < 2r_i$, drives the outflow. In fact, we found that the size of the disk that participates in the wind is simply determined by

$$\beta_d \leq 1.0. \quad (5.31)$$

⁸ Our results show that an episodic behavior of the jet is possible independently of the underlying disk or central object.

On using equation (2.16), this becomes

$$r_{\text{wind}} \leq r_1 = (\frac{2}{5}\beta_i \delta)^{2/5} \simeq 4r_i \quad (5.32)$$

for our parameters, in agreement with our simulation. To be more concise, the outflow is triggered when a toroidal magnetic field is generated at the shear between the disk and corona at $\tau = 0$ and then propagates to larger z via a torsional Alfvén wave. Because of the higher Kepler shear, the strongest toroidal field is generated in the inner regions of the disk (where β is also high). Thus, a radial, outwardly directed magnetic pressure gradient is produced by the newly created toroidal field. This pushes open the field lines setting up a condition favorable for outflow. This is shown in Figure 9, which plots the ratio $|B_\phi|/B_p$ versus the poloidal magnetic structure. Because $|B_\phi|/B_p \simeq 20$ in the inner parts of the disk and only $|B_\phi|/B_p \simeq 0.4$ in the outer parts, a strong magnetic pressure gradient opens up the field lines into a configuration favorable for a wind to be ejected. This ejection is seen in Figure 10, where we see that the magnetic pressure gradient, $\nabla(B_\phi^2)$, not only opens up the initial con-

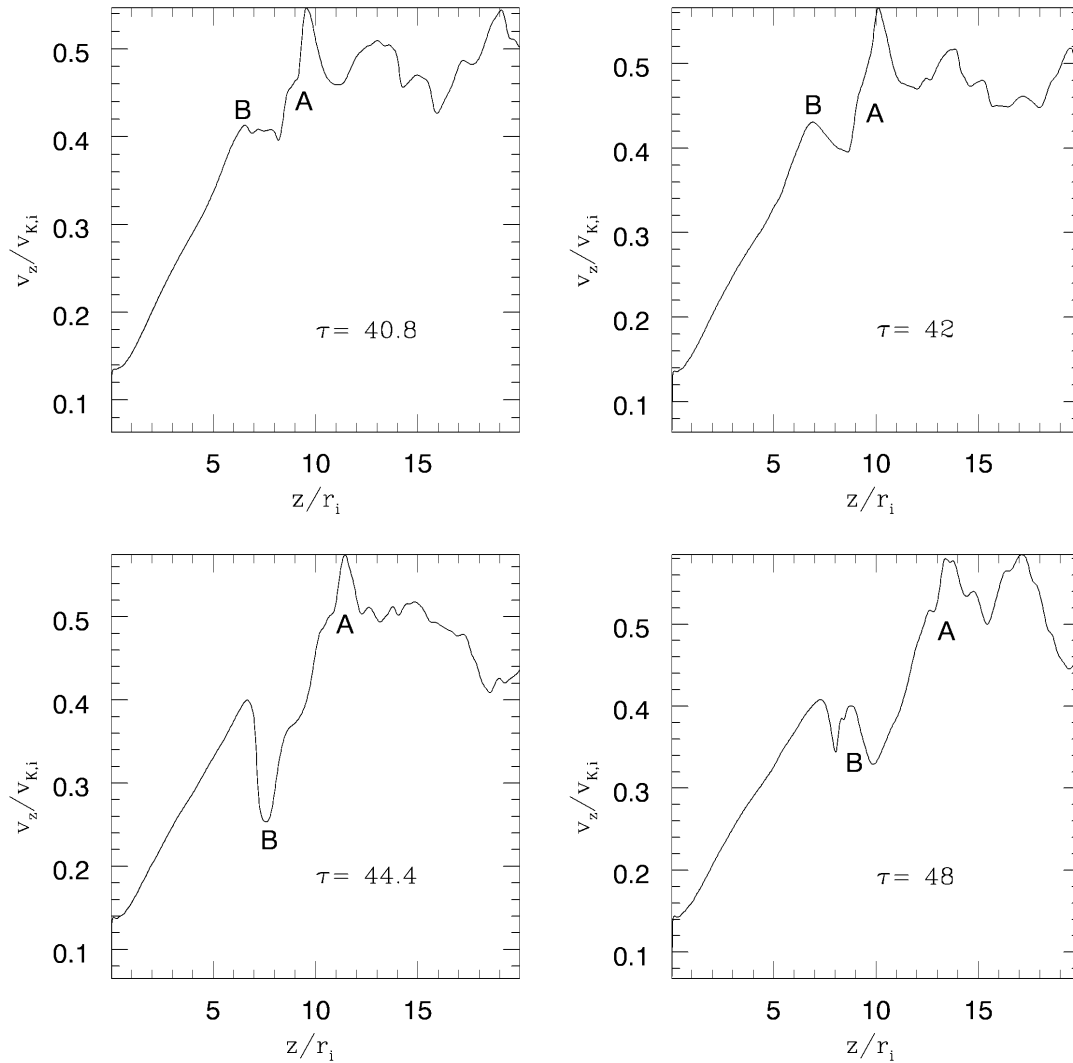


FIG. 7b

figuration but also clears up the immediate surrounding corona.

For $r \geq r_1$ (or $\beta_d \leq 1.0$), the field is more rigid as one moves radially so that this determines the radial extent of the ejection region. That is, the wind production region on the surface of the disk depends on the ease with which field lines can be pushed aside by the toroidal field pressure (Ouyed & Pudritz 1997b).

5.1. Centrifugal Outflow

In general, the physics of how a flow starts and is accelerated is dictated by the interplay between three forces. The gas is then centrifugally accelerated along the open structure and quickly becomes collimated by the self-generated Lorentz force $\mathbf{J}_p \times \mathbf{B}_\phi$.

Figure 11 displays the evolution of the Alfvén surface as the knots are being generated. One sees that the Alfvén surface remains fixed in space and there achieves a steady state. That is, we have found two regions to our episodic outflow: the acceleration region (interior to the Alfvén surface), where the physics is very steady and stable; and the knot region (beyond the Alfvén surface), where the flow becomes episodic. The FM surface turned out to be very

complicated and unsteady as it gets sometimes destroyed by the knots.

In order to investigate the stationary region, interior to the Alfvén surface, we applied the steady state analysis package introduced in OPI. That is, for the field lines involved in the outflow, we estimated the two corresponding BP82 parameters κ (characterizing the ratio of the mass flux to the magnetic flux) and λ (the total specific angular momentum). We then plot (Fig. 12) the standard κ - λ graph (upper panel) and the κ - θ_0 graph (lower panel) with the location of the launching angle θ_0 . As can be seen in the κ - λ figure, the outflow is clearly particle dominated ($\kappa \geq 1$) and one expects such flows to be dominated by rotation, unlike the magnetically dominated outflow obtained in OPI where $\kappa < 1$.

6. JET FLUXES

Finally, we quantify, in Figure 13, the strength of our simulated large-scale outflow (simulation A; see OPI for the units). The quantities of observational interest are the mass flux, the momentum flux and the kinetic flux. The solid line denotes the fluxes across the inner ($z = 0.0$) boundary. The dotted line denotes the fluxes across the outer axial bound-

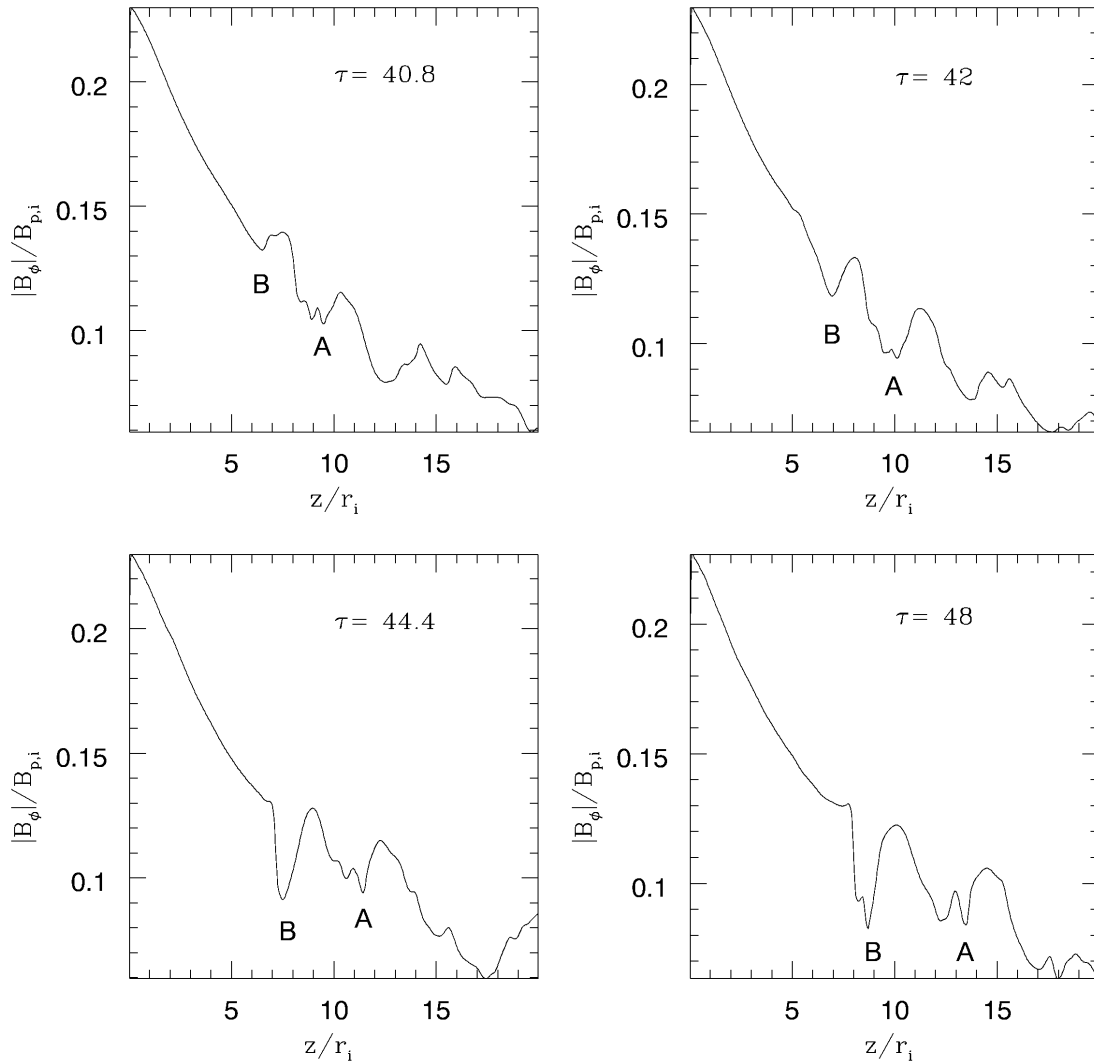


FIG. 7c

ary ($z = 80.0$). The fluxes across the outer radial boundary ($r = 20.0$) are negligible (hardly any matter leaves the outer radial boundary). At later times, the fluxes in the outflow are comparable to the fluxes at the inner boundary. When given in cgs units (and assuming values for the free parameters appropriate to a protostellar disk and/or black holes), then the typical mass, momentum, and energy flux rates are given in Table 5. While these fluxes are small when compared to the results of the steady state simulation (a factor of 3) (OPI), they are still capable of providing enough

TABLE 5
JET ENERGETICS

Central Object	Mass (M_{\odot})	\dot{m}_w ($M_{\odot} \text{ yr}^{-1}$)	$\dot{m}_w v$ ($M_{\odot} \text{ km s}^{-1} \text{ yr}^{-1}$)	$\dot{m}_w v^2$ (ergs s^{-1})
Protostar	0.5	3.04×10^{-7}	1.42×10^{-5}	1.25×10^{32}
Black hole	10^8	1.41×10^{-2}	3.71×10^2	1.92×10^{43}

momentum to drive the observed weak CO outflows⁹ (Lada 1985; Chernin & Masson 1991). Figure 14 quantifies the bulk energies involved in our flow (integrated over the entire large-scale computing volume). It shows that our solution, unlike the stationary one (OPI), corresponds to a flow in which most of the energy is in the form of the bulk toroidal kinetic energy (*lower panel*). This is a result that is expected since our flow is particle dominated (rotating flow since $\kappa \geq 1$, as explained in § 5.1).

Finally, in Figure 15a, we show a snapshot (at $\tau = 400$) of the dependence of the mass outflow rate upon the poloidal velocity of the jet for the large-scale simulation. The top panel shows that the velocity peaks in two dominant

⁹ One still needs to carry out simulations at much larger scales (CO scales) to make any definite conclusions about the energetics of our outflows far from the source. Note that molecular outflows cannot be simulated with the code. Our conclusion is based on the assumption of the energy and momentum transfer between our atomic outflows and the molecular ambient cloud.

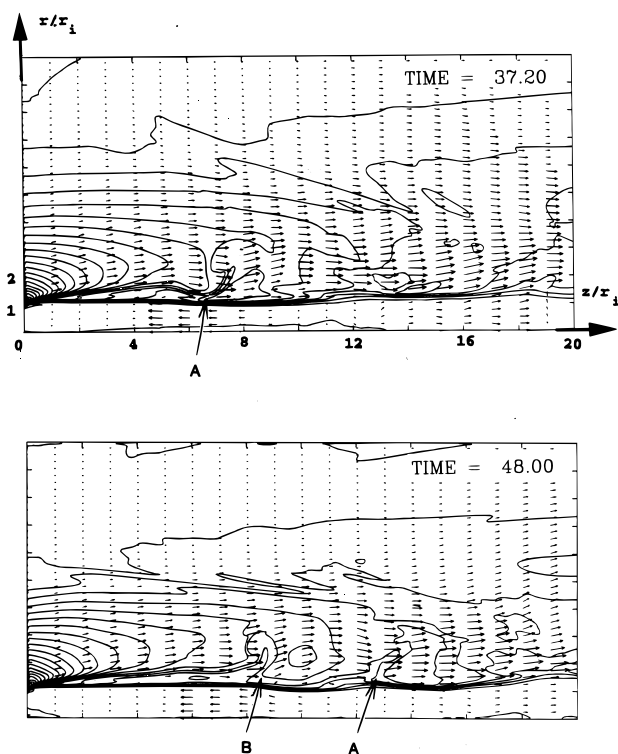


FIG. 8.—Poloidal vector velocity (v_p) and isocontours of the toroidal magnetic field (B_ϕ) at $\tau = 37.2$ and $\tau = 48.0$. 20 linearly spaced contours are shown for B_ϕ . As the flow recollimates toward the axis, it then reflects back into the slower moving body of the jet. Generally speaking, high-velocity regions (associated with the knots) are associated with regions of low toroidal field strength.

streams ($r \simeq 1.5r_i$ and $r \simeq 7r_i$). The middle panel confirms the fact that most of the material is carried out in the range $r_i < r_{\text{wind}} < 8r_i$. That is, while the gas is ejected from the $r_i < r_{\text{wind}} < 2r_i$ region on the disk surface, as it evolves, it reaches a width of about $7r_i$. The lower panel indicates that the bulk of the material moves at small speeds ($\simeq 0.15v_{K,i}$), while much smaller amounts of diffuse gas move at high speed ($\simeq 0.2v_{K,i}$). Note that Fig. 15a is taken at a snapshot time during which the highest velocities registered were low ($\simeq 0.2v_{K,i}$). However, velocities as high as $0.7v_{K,i}$ are reached in our flow. Figure 15b is similar to Figure 15a except that it is for the small-scale simulation and the snapshot is taken at $\tau = 40$. Here, we reach velocities as high as $0.5v_{K,i}$ but still confirm that the bulk of the material moves at small speeds ($\simeq 0.2v_{K,i}$). While this last result is in reasonable agreement with large-scale observations,¹⁰ one needs data at scales comparable to the ones we are simulating in order to make any definite conclusions.

7. CONCLUSION

In this paper, we have presented results from a numerical study of the origin and the evolution of winds from accretion disks threaded by vertical field lines. The main points discovered in our present work can be summarized as follow:

¹⁰ It is observed in CO outflows that almost all the material is traveling at relatively small speeds ($10\text{--}30\text{ km s}^{-1}$), and only a small fraction has a velocity near the observed maximum value (300 km s^{-1}). See Fig. 2 in Masson & Chernin (1992).

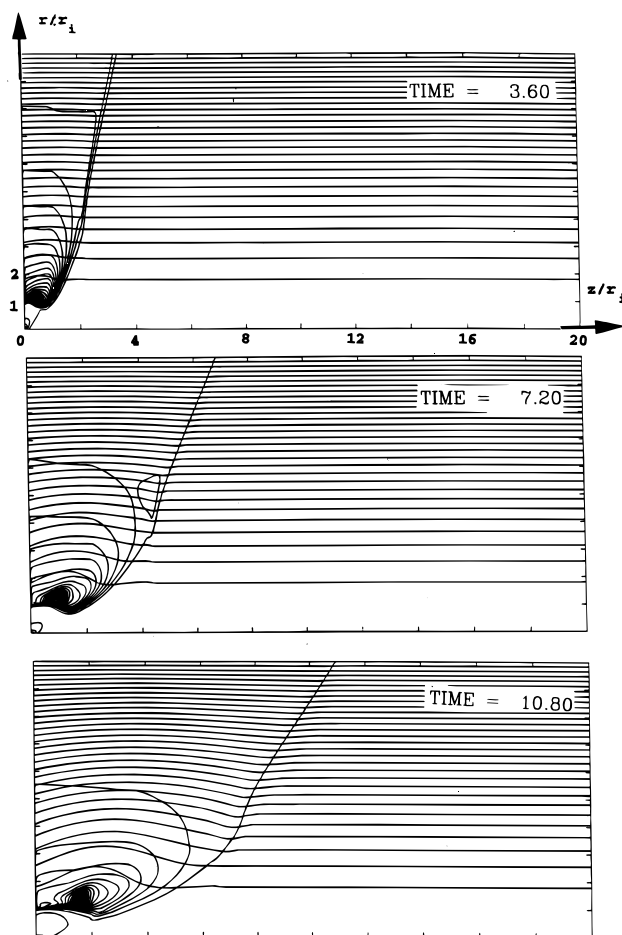


FIG. 9.—Twenty linearly spaced contours for B_ϕ/B_p . The corresponding $V(B_\phi^2)$ force opens up the initially vertical magnetic configuration. In the inner parts of the disk, where $|B_\phi|/B_p \simeq 20.0$, the nonlinear torsional Alfvén waves control most of the dynamics. Here $\tau = 3.6$, $\tau = 7.2$, and $\tau = 10.8$, from top to bottom.

1. *Self-starting jets.*—For our initial magnetic field structure, conditions favorable for ejection set themselves up automatically through the flow of nonlinear torsional Alfvén waves that builds a radially directed, toroidal magnetic pressure gradient that adjusts the structure of the coronal field. We found that vertical magnetic configuration with a coronal β of order of unity in the inner parts of the disk is most favorable for the formation of episodic jets. The flow is centrifugally ejected from the portion of the disk surface where the magnetic field lines have opened to less than the critical angle ($\simeq 60^\circ$), as expected from the centrifugally driven wind theory.

2. *Knots and the knot generator.*—While there are models for the formation of episodic jets that involve eruptions in time-variable accretion disks (Stone & Norman 1994; Raga & Koffman 1990), our simulations show that this is not necessarily required. We found that the knot generator is inherent to the jets themselves and produces eruptions that might explain the episodic events observed on much larger scales than what is simulated here. The knot generator is fixed in space and is simply the strong toroidal magnetic field generated that by recollimating the flow toward the disk's axis produces knots through magnetohydrodynamic (MHD) shocks. The knots produced are not related to any of the known classic instabilities.

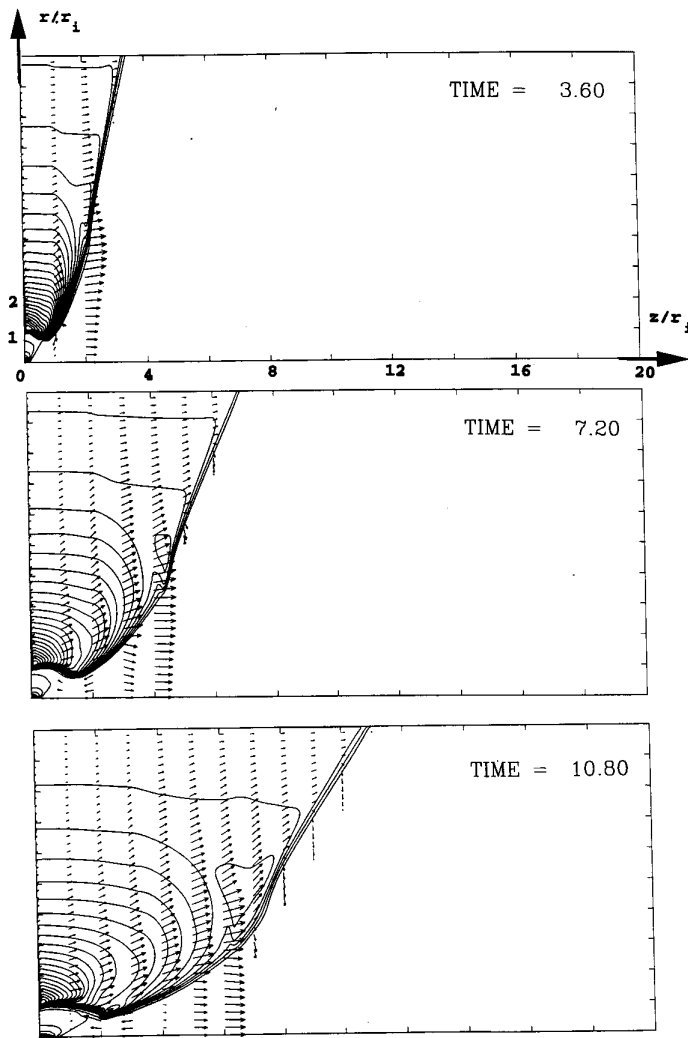


FIG. 10.—Major role played by the $\nabla(B_p^2)$ force (20 linearly spaced contours are shown for B_p) as it clears up the immediate surroundings of the disk. A wind is centrifugally ejected from the inner most field lines. Here $\tau = 3.6$, $\tau = 7.2$, and $\tau = 10.8$, from top to bottom.

3. *Disk surface.*—We hypothesize that real physical systems are episodic because the physics of their central accretion disks leads typically to situations where the threading mean magnetic fields are such that the β in the surface of the disk decreases with the disk radius. It is still too early to tell whether or not this condition naturally arises in models of accretion disks that have MHD turbulence. The rigidity of such a magnetic structure determines the portion of the disk that participates in the flow.

4. *Terminal velocities.*—The outflow velocities achieved are still too small (by a factor of 2) to match the slowest structures seen in observed YSO jets. However, one has to remember that our two simulations, while typical of several dozen that we have carried out, still probe only a small part of parameter space. Large-scale simulations will certainly help in studying the evolution of the flow farther away from the source.

Our conclusions must be tempered by several assumptions we have made. For example, we have assumed axisymmetry and that the thermodynamics is polytropic. We have also assumed ideal MHD. Finally, let us mention that the primary effect of reducing the dimensionality of the

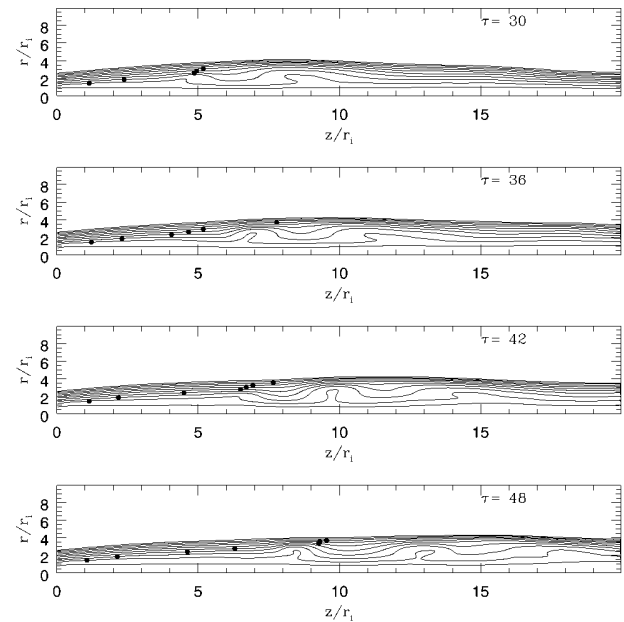


FIG. 11.—Evolution of the Alfvén surface. This shows that throughout the strongly episodic outflow, the Alfvén surface stays fixed in space.

dynamics is to eliminate some modes of MHD instabilities. These modes can play an important role in the dynamics of such winds. It is clear that investigating the effects of the missing physics cited above on astrophysical jets is an important avenue for future research.

We thank Jim Stone, David Clarke, and Patricia Monger for all the help and support during the course of this project and an anonymous referee for remarks that helped to clarify some of the discussion. R. O. acknowledges the financial support of McMaster University. The research grant of R. E. P. is supported by a grant from the Natural Science and Engineering Research Council of Canada.

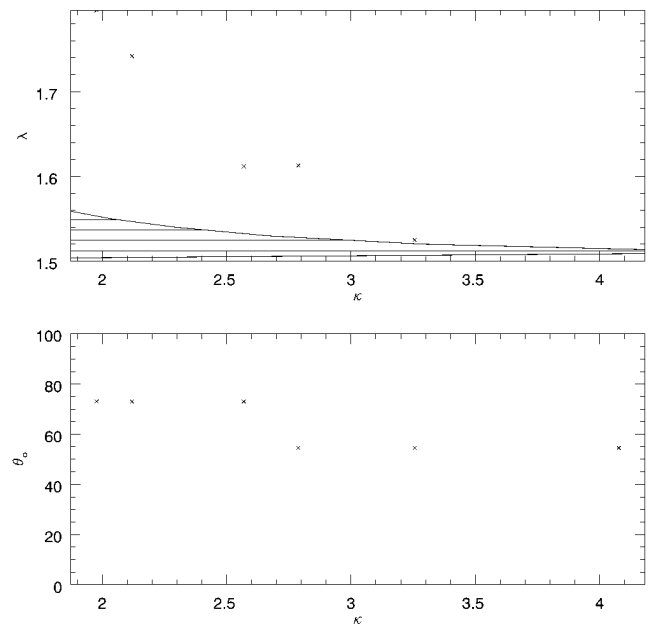


FIG. 12.—The κ - λ space (upper panel) and the κ - θ_0 space (lower panel) and the location of our solution, at $\tau = 400$. Our solution is a particle-dominated jet with $\kappa \geq 1$. In the upper panel, the dashed area represents the sub-Alfvénic flows [$4\pi\rho v_p^2 < B_p^2$ or $\kappa\lambda(2\lambda - 3)^{1/2} < 1$].

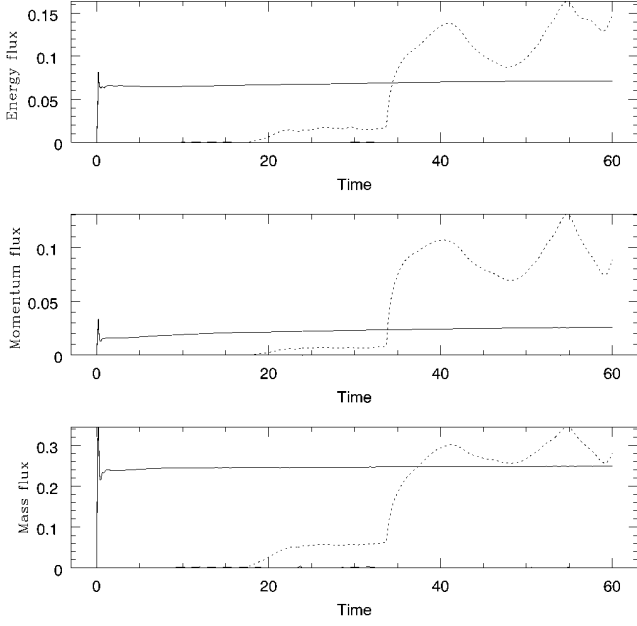


FIG. 13.—Here, we quantify the different fluxes carried by the jet. The bottom panel represents the mass flux, the middle panel represents the momentum flux, while the top panel represents the kinetic flux. The solid lines denote the fluxes across the inner ($z = 0$) boundary. The dotted lines denote the fluxes across the outer axial boundary ($z = z_o$). The fluxes across the outer radial boundary ($r = r_o$) are negligible (hardly any matter leaves the outer radial boundary). Note the effect of the knotty structure on the flow crossing the outer axial boundary (*dotted line*).

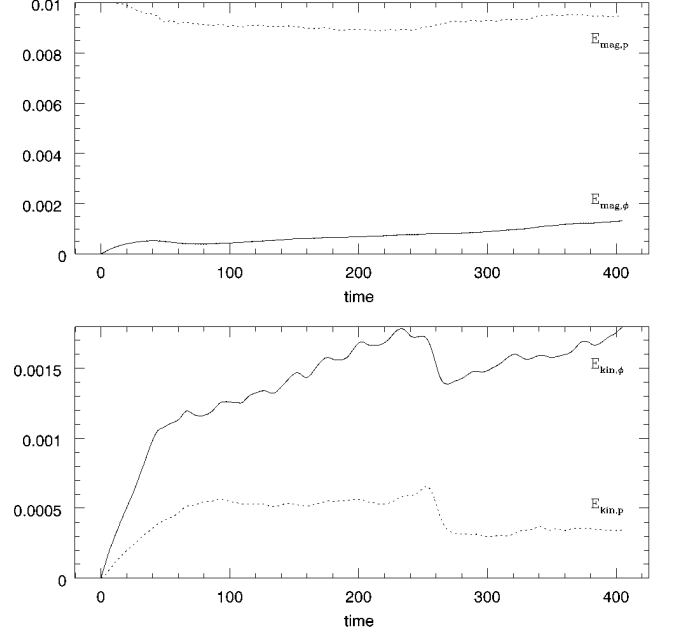


FIG. 14.—Quantification of the energies involved in the flow. In the upper/lower panel, the poloidal magnetic/kinetic energy is compared to the toroidal part.

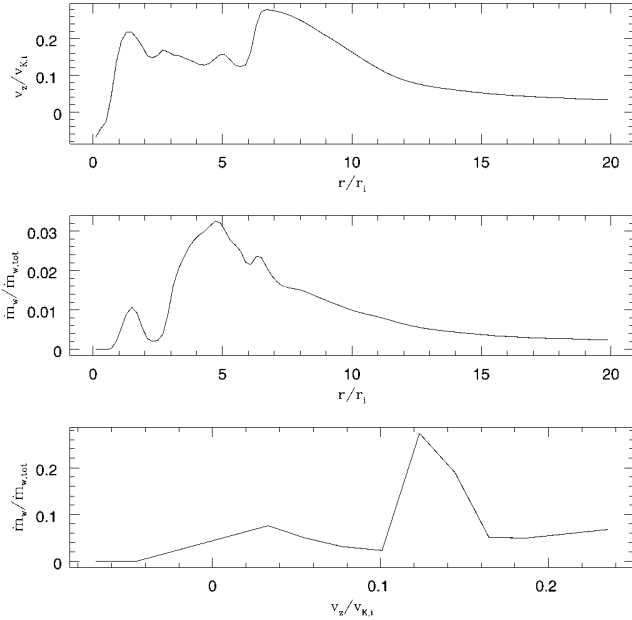


FIG. 15a

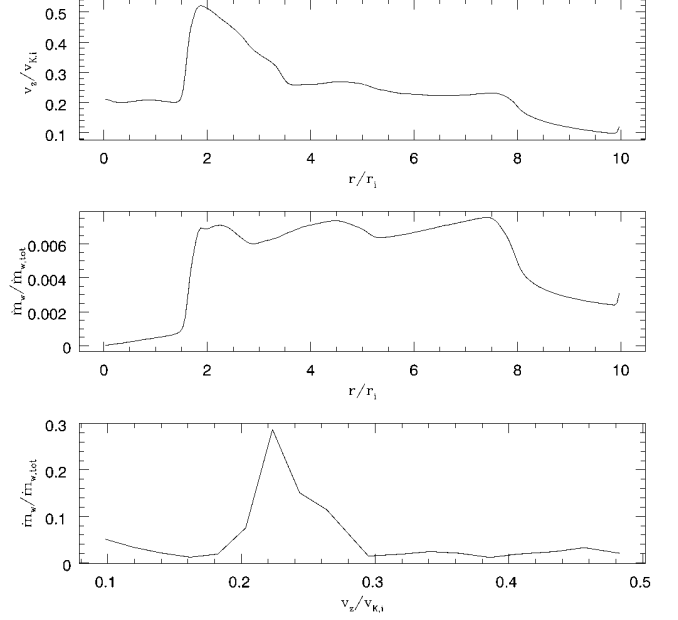


FIG. 15b

FIG. 15.—(a) Simulation A. A snapshot (at $\tau = 400$) of the dependence of the mass outflow rate upon the poloidal velocity of the jet (*lower panel*). The top panel shows that the velocity peaks in two dominant streams ($r \simeq 1.5r_i$ and $r \simeq 7r_i$). The middle panel shows the width of the outflow ($1r_i < r_{\text{wind}} < 8r_i$) as it evolves above the disk's surface. Note, however, that only a small portion of the disk ($1r_i < r_{\text{wind}} < 2r_i$) ejects a wind. (b) Simulation B. A snapshot (at $\tau = 40$) of the dependence of the mass outflow rate upon the poloidal velocity of the jet (*lower panel*). The top panel shows that the velocity peaks in two dominant streams ($r \simeq 1.5r_i$ and $r \simeq 4.5r_i$). The middle panel confirms the width of the outflow ($1r_i < r_{\text{wind}} < 8r_i$).

REFERENCES

- Appl, S., & Camenzid, M. 1992, *A&A*, 256, 354
 Balbus, S. A., & Hawley, J. F. 1991, *ApJ*, 376, 214 (BH)
 Bell, A. R., & Lucek, S. G. 1995, *MNRAS*, 277, 1327
 Birkinshaw, M. 1990, in *Beams and Jets in Astrophysics*, ed. P. A. Hughes (Cambridge: Cambridge Univ. Press), 278
 Blandford, R. D., & Payne, D. R. 1982, *MNRAS*, 199, 883 (BP82)
 Calvet, N., Hartmann, L., & Kenyon, S. J. 1993, *ApJ*, 402, 623
 Camenzid, M. 1987, *A&A*, 184, 341
 Chernin, L. M., & Masson, C. R. 1991, *ApJ*, 382, L93
 Clarke, D. A., Norman, M. L., & Burns, J. O. 1986, *ApJ*, 311, L63
 Eislöffel, J., & Mundt, R. 1994, *ApJ*, 284, 530
 Ferreira, J., & Pelletier, G. 1995, *A&A*, 295, 807
 Frank, J., King, A. R., & Raine, D. J. 1992, *Accretion Power in Astrophysics* (Cambridge: Cambridge Univ. Press)
 Heyvaerts, J., & Norman, C. 1989, *ApJ*, 347, 1055
 Königl, A. 1989, *ApJ*, 342, 208
 Königl, A., & Ruden, S. P. 1993, in *Protostars and Planets III*, ed. E. H. Levy & J. I. Lunine (Tucson: Univ. of Arizona Press), 641
 Kössl, D., Müller, E., & Hillebrandt, W. 1990, *A&A*, 229, 378
 Lada, C. J. 1985, *ARA&A*, 23, 267
 Li, Z.-Y. 1995, *ApJ*, 444, 848
 Lind, K. R., Payne, D. G., Meier, D. L., & Blandford, R. G. 1989, *ApJ*, 344, 89
 Lovelace, R. V. E., Wang, J. C. L., & Sulkanen, M. E. 1987, *ApJ*, 315, 504
 Lubow, S. H., Papaloizou, J. C. B., & Pringle, J. E. 1994, *MNRAS*, 268, 1010
 Masson, C. R., & Chernin, L. M. 1992, *ApJ*, 387, L47
 Mouschovias, T. Ch., & Paleologou, E. V. 1980, *ApJ*, 237, 877
 Ouyed, R., & Pudritz, R. E. 1993, *ApJ*, 419, 255
 ———. 1994, *ApJ*, 423, 753 (OP94)
 ———. 1997a, *ApJ*, 482, 712
 ———. 1997b, in preparation
 Ouyed, R., Pudritz, R. E., & Stone, J. M. 1997, *Nature*, 385, 409
 Pelletier, G., & Pudritz, R. E. 1992, *ApJ*, 394, 117
 Pudritz, R. E., & Norman, C. A. 1986, *ApJ*, 301, 571
 Raga, A. C., & Kofman, L. 1992, *ApJ*, 386, 222
 Reipurth, B. 1989, in *Low Mass Star Formation and Pre-Main-Sequence Objects*, ed. B. Reipurth (Garching: ESO), 247
 Reys-Ruis, M., & Stepinski, T. 1996, *ApJ*, 459, 653
 Sauty, C., & Tsinganos, K. 1994, *A&A*, 287, 893
 Shibata, K., & Uchida, Y. 1986, *PASJ*, 38, 631
 Stone, J. M., & Norman, M. L. 1994, *ApJS*, 433, 746
 Uchida, Y., & Shibata, K. 1985, *PASJ*, 37, 515
 Ustyugova, G. V., Koldoba, A. V., Romanova, M. M., Chechetkin, V. M., & Lovelace, R. V. E. 1995, *ApJ*, 439, L39
 Wardle, M., & Königl, A. 1993, *ApJ*, 410, 218